ADVANCED MATERIALS
www.advmat.de

Magnetic Domain Texture in Fe_3O_4 Thin Films on SiO_2 Nanospheres

Mai Hussein Hamed, Yifan Xu, Hebatalla Elnaggar, Mohamed Zaghloul, Antonio M. Mio, Alicia Backs, Annika Stellhorn, Vitor de Oliveira Lima, Chenyang Yin, Connie Bednarski-Meinke, Nina-Juliane Steinke, Oleg Petracic, Thomas Brückel, Thomas Saerbeck, and Asma Qdemat**

Topographically complex interfaces offer a promising route to engineer magnetic textures in oxide thin films, with potential implications for next-generation spintronic and neuromorphic devices. Here, Fe_3O_4 thin films are grown on self-assembled SiO_2 nanospheres to investigate how local curvature, together with polycrystalline morphology, influence magnetic behavior compared to flat films. STEM and GISANS confirm connected growth with preserved lateral ordering, while XMCD-PEEM reveals in-plane magnetic domains that extend across both nanosphere-patterned and flat regions. Despite the low net magnetization of the Fe_3O_4 caps, their domain orientations align with neighboring flat areas, indicating correlated domain behavior across structurally different regions. These findings demonstrate how nanoscale topography and morphology can be leveraged as design parameters to modulate magnetism in complex oxides.

1. Introduction

The emerging field of curvilinear spintronics explores how geometric curvature and topology to modulate magnetic properties beyond what is possible in flat films.[1,2] Recent studies have shown that placing magnetic materials into 3D geometries–such as spheres, cylinders, coils, or helical surfaces–induces novel magnetic effects.[3,4] These include domain wall pinning, magnetization reversal, and curvature-induced anisotropy.[5,6] Additionally, curvature-induced morphological modifications–strain, thickness gradients, and modified exchange interactions–can stabilize unique spin textures, such as skyrmions, and vortex states, offering significant advantages for energy-efficient computing.[7–9] Curvature has also been shown to influence exchange bias, interfacial magnetic coupling, and spin transport, enhancing the tunability of magnetoelectric and magneto-optic functionalities.[7,10,11] While such effects have been demonstrated across a wide range of material systems, including transition metal oxides, perovskites, and magnetic multilayers[12–14]–the role of geometry in oxide-based thin films remains relatively unexplored.

M. H. Hamed, Y. Xu, V. de O. Lima, C. Yin, C. Bednarski-Meinke, O. Petracic, T. Brückel, A. Qdemat[+]
Forschungszentrum Jülich GmbH
Jülich Centre for Neutron Science (JCNS-2)
JARA-FIT, 52425 Jülich, Germany
E-mail: Mai.hussein@science.helwan.edu.eg; qdematai@ornl.gov

M. H. Hamed
Helwan University
College of Science
Cairo 4037120, Egypt

The ORCID identification number(s) for the author(s) of this article can be found under https://doi.org/10.1002/adma.202513849

[+]Present address: Neutron Scattering Division, Oak Ridge National Laboratory, Oak Ridge TN 37831, USA

DOI: 10.1002/adma.202513849

Y. Xu, C. Yin, O. Petracic
Heinrich Heine University Düsseldorf
Faculty of Mathematics and Natural Sciences
40225 Düsseldorf, Germany

H. Elnaggar
Institute of Mineralogy
Physics of Materials and Cosmochemistry, CNRS
Sorbonne University
4 Place Jussieu, Paris 75005, France

M. Zaghloul, A. M. Mio
Institute for Microelectronics and Microsystems (IMM)
Consiglio Nazionale delle Ricerche (CNR)
Strada VIII N. 5, Catania 95121, Italy

A. Backs, A. Stellhorn
European Spallation Source ERIC
Partikelgatan 2, Lund 224 84, Sweden

V. de O. Lima
RWTH Aachen
Faculty of Mathematics, Computer Science and Natural Sciences
52074 Aachen, Germany

N.-J. Steinke, T. Saerbeck
Institut Laue-Langevin
71 Avenue des Martyrs, Grenoble Cedex 9 CS 20156, France

In conventional flat in-plane magnetic oxide thin films, research has primarily focused on enhancing the magnetic properties through interface engineering, aiming to optimize electric and magnetic switching mechanisms, strain, or interfacial polarization for use in tunable neuromorphic computing systems.[15,16] However, recent work suggests that geometric design is a powerful parameter in curvilinear spintronics, where curvature-induced magnetic modulation can enhance the performance and functionality of spintronic devices.[6,7,17] This is especially relevant for neuromorphic computing systems, which require low-power, re-configurable, and stable operation.[18] Within this context, curved magnetic films present a particularly promising platform by integrating intrinsic material properties with curvature-induced effects such as strain modulation, spin texture stabilization, and domain wall engineering, offering enhanced tunability for next-generation spintronic and neuromorphic technologies.[19–21]

Among these magnetic oxides, magnetite (Fe_3O_4) is of particular interest due to its high spin polarization and tunable electronic and magnetic properties.[22–24] Fe_3O_4 features an inverse spinel structure in which Fe^{2+} and Fe^{3+} ions occupy distinct lattice sites, giving rise to its ferrimagnetic and half-metallic properties. It has a Curie temperature of 860 K and a saturation magnetization of $4\mu_B$ per formula unit,[25] making it an attractive candidate for room temperature oxide spintronics. While flat Fe_3O_4 thin films have been widely studied, the influence of three-dimensional nanoscale curvature on their magnetic properties remains largely unexplored. Our previous work has shown that oxide interfaces in Fe_3O_4-based systems can be tuned magnetically and electrically via the surface chemistry supported by the active role of the oxide substrate,[26–28] pointing to strong sensitivity to local structure environment. With these findings as a starting point, we now look at how nanoscale topographic complexity can affect magnetic properties in Fe_3O_4-based systems.

In this study, we investigate how nanoscale topography modulates magnetism in Fe_3O_4 thin films grown on self-assembled SiO_2 nanospheres supported by Nb-doped $SrTiO_3$ substrates. These nanospheres provide a periodic, quasi-3D surface topography that introduces lateral thickness variations and local curvature, while maintaining epitaxial growth in surrounding flat regions that significantly impact magnetic domain formation, interfacial coupling, and magnetization reversal mechanisms. Using advanced structural and magnetic characterization techniques, we systematically examine how these three-dimensional surface features influence (1) thickness variation, (2) magnetic and chemical interface structure, and (3) induced domain texture through correlated domain behavior. By studying the interplay between nanoscale morphology and magnetism, our findings advance the understanding of geometry-mediated effects in oxide-based magnetic materials and identify nanosphere-templated films as promising platforms for geometry-driven magnetic engineering in curvilinear and neuromorphic spintronics.

2. Results and Discussion

To investigate the effect of nanoscale topography on the magnetic and structural properties of Fe_3O_4 films, we grow 24±2 nm thick films on both flat Nb-doped $SrTiO_3$ (Nb:STO) substrates and self-assembled SiO_2 nanospheres (174±7 nm diameter) using pulsed laser deposition (PLD). The growth conditions were chosen based on our previous studies[26–28] to ensure the formation of the magnetite (Fe_3O_4) phase. For detailed growth parameters and film characterization techniques, see Section 4: Experimental Details.

2.1. Local Surface Structure: SEM

To analyze the surface morphology and ordering of the nanospheres before and after film deposition, scanning electron microscopy (SEM) images were taken from several locations on the sample under various magnifications. The SEM images chosen here, shown in **Figure 1**a–c, represent part of the surface characteristics of SiO_2 nanospheres on Nb-doped TiO_2-terminated $SrTiO_3$ (001) (Nb:STO) substrate. The SEM images reveal that the top surface primarily exhibits a 2D hexagonal arrangement, with occasional square patterns highlighted in yellow in Figure 1b. This hexagonal ordering is further confirmed by the distinct pattern of sharp spots in the Fast Fourier Transform (FFT) inset of Figure 1a.

SEM images acquired after the growth of the Fe_3O_4 film are shown in Figure 1d–f. The FFT in the inset of Figure 1d shows a transition from a highly ordered nanosphere arrangement to a structure with reduced local order. This is attributed to the Fe_3O_4 film filling the gaps between the spheres. However, the overall structure remains largely intact, with hexagonal arrangements still dominating. Furthermore, the contrast variation in Figure 1f indicates the formation of Fe_3O_4 caps on the top surfaces of the nanospheres. These caps are formed as a result of the deposition process, where the film conforms to the curved surface of the nanospheres.

While SEM of Fe_3O_4 film on the SiO_2 nanospheres reveals the surface morphology of the system, it cannot resolve the interfacial atomic structure between the Fe_3O_4 film and the nanospheres. To gain this information, we applied scanning transmission electron microscopy (STEM), which provides atomic-resolution cross-sectional images of the film at various interface regions, as discussed in the next section.

2.2. Local Depth-Resolved Structure: STEM

A scanning transmission electron microscopy (STEM) micrograph using Low-Angle Annular Dark Field (LAADF) of a cross-section of the Fe_3O_4 film on SiO_2 nanospheres deposited on Nb:STO substrate sample is shown in **Figure 2**a. It offers a detailed view, showing variations in Fe_3O_4 film thickness on a single SiO_2 nanosphere. A uniform cap with a roughly smooth surface is forming on the nanospheres with a thickness variation from the top of the spheres to the edges. Some other parts of the Fe_3O_4 film are directly deposited on the Nb:STO substrate in exposed substrate areas between the nanospheres. Other parts of the film are deposited in the space between adjacent nanospheres to form a continuous coverage of Fe_3O_4 film on the nanospheres.

In the selected area electron diffraction (SAED) of Area 2 in Figure 2c), the Fe_3O_4 film on the Nb:STO (100) substrate exhibits a single-crystal structure aligned along the <100 > direction as demonstrated by the diffraction patterns which shows double-peak formation refer to the epitaxial growth of the film on the

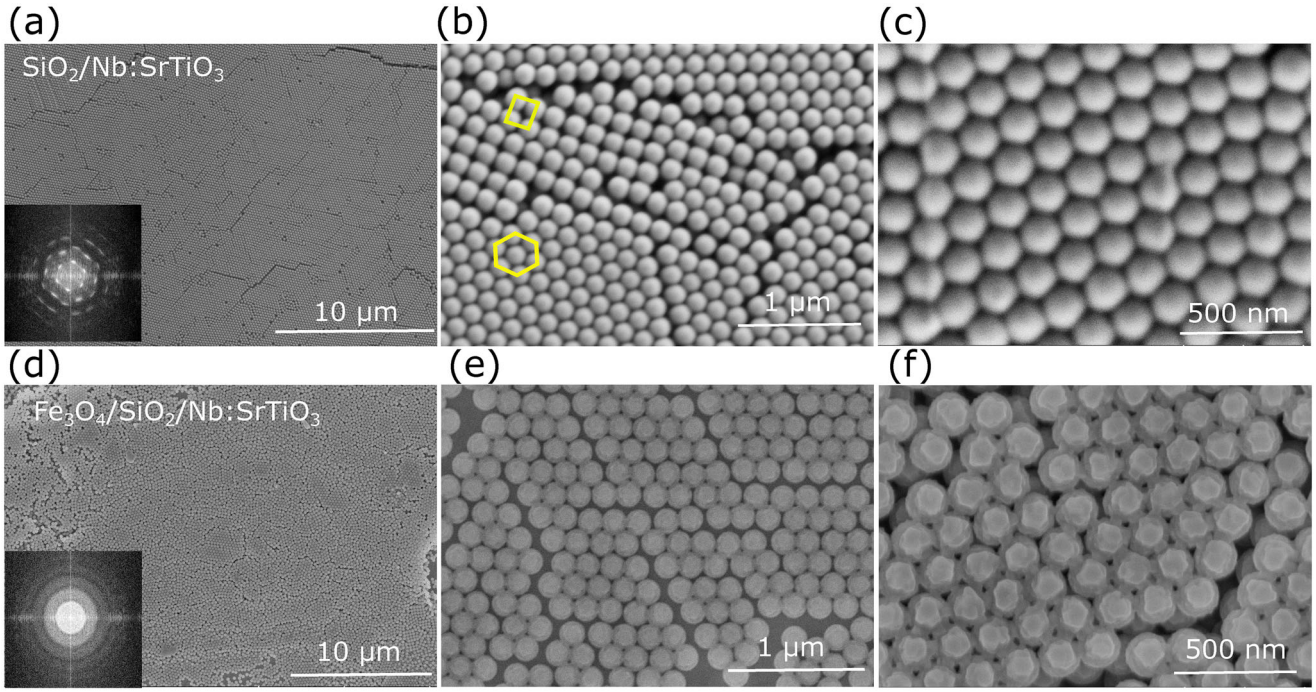

Figure 1. SEM images of (a–c) SiO_2 nanospheres and (d–f) Fe_3O_4 film on SiO_2 nanospheres with different magnifications, insets represent Fast Fourier Transform (FFT) of the images.

substrate, where the substrate diffraction is shown in Figure 2b. No diffraction spots are observed in Area 3 (Figure 2d), confirming the amorphous nature of the nanospheres. The Fe_3O_4 film on the amorphous SiO_2 nanospheres in Area 4 (Figure 2e) is polycrystalline, where diffraction spots indicate the absence of alignment.

Figure 2f shows a High-Angle Annular Dark Field (HAADF) STEM micrograph of the Fe_3O_4 film on SiO_2 nanospheres (for comparison with a flat Fe_3O_4 film on Nb:STO, see Figure S2, Supporting Information). In the nanosphere region, the micrograph shows a combination of bright and dark contrast at the interface between the film and the spheres. Since HAADF is sensitive to the atomic number (Z), and Fe has a higher atomic number, the Fe_3O_4 appears brighter than SiO_2. This contrast could suggest structural, chemical or morphological intermixing at the interface. However, given the 3D geometry of the nanospheres and the projection nature of STEM imaging, it is also possible that the observed contrast arises from superposition of signals from the front and back surfaces of the TEM lamella cutting the curved spheres. This effect is noticeable near the edges of the nanospheres, as seen in Figure 2a. Therefore, the observed contrast at the interface may result from either material intermixing or 3D projection artifacts introduced by the spherical morphology.

Taken together, plane-view SEM and cross-sectional STEM demonstrate that the Fe_3O_4 film forms polycrystalline nanocaps

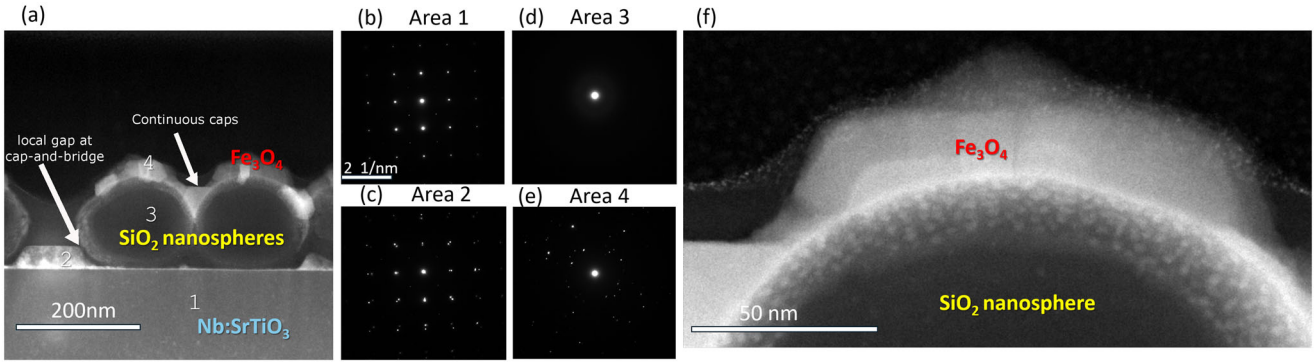

Figure 2. Cross-sectional micrographs of Fe_3O_4 film on SiO_2 nanospheres: a) LAADF STEM micrograph of SiO_2 nanospheres coated with the Fe_3O_4 film, b–e) Diffraction patterns from the regions marked in (a) in the $SrTiO_3$ [001] zone axis: Area 1 $SrTiO_3$ substrate, Area 2 single crystalline Fe_3O_4 film on $SrTiO_3$ (100) with epitaxial growth, Area 3 Amorphous SiO_2 nanospheres, and Area 4 polycrystalline Fe_3O_4 film on SiO_2 nanospheres. f) HAADF STEM micrograph of Fe_3O_4 film on SiO_2 nanospheres.

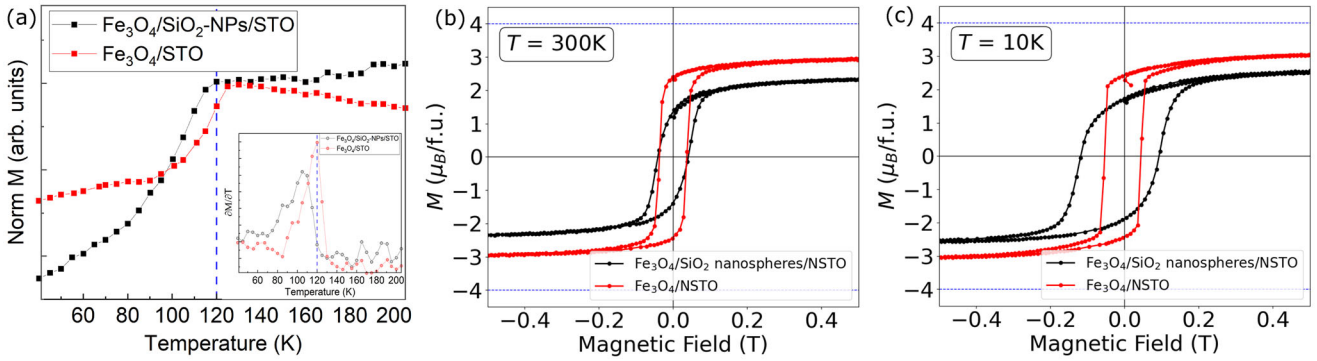

Figure 3. a) Magnetization vs. temperature curve at a magnetic field of 0.05T for Fe_3O_4 film deposited on SiO_2 nanospheres on Nb:STO substrate and reference Fe_3O_4 film on flat Nb:STO substrate with inset showing the first derivative for the magnetization curve to determine the Verwey transition. b,c) Magnetization vs magnetic field for Fe_3O_4 film deposited on SiO_2 nanospheres on Nb:STO substrate and reference Fe_3O_4 film on flat Nb:STO substrate at temperatures of 300 and 10K, respectively.

interconnected by interstitial bridges (Figures S5 and S6, Supporting Information). This quasi-continuous cap-and-bridge network, with local gaps at the curved–flat interfaces, spans both flat substrate regions and curved nanosphere surfaces, rather than an ensemble of isolated nanoparticles. This morphology is therefore more accurately described as an almost continuous thin film with local curvature variations, where both curvature and polycrystalline grain structure contribute to the observed structural and magnetic properties.

These structural insights provide a foundation for understanding how the local morphology and crystallinity of the Fe_3O_4 film influence its magnetic properties. To correlate these structural features with the magnetic response of the system, we now turn to magnetic and scattering measurements, including vibrating sample magnetometer (VSM), polarized neutron reflectivity (PNR), and polarized grazing-incidence small-angle neutron scattering (GISANS) analyses, which will be discussed in the following sections.

2.3. Global In-Plane Magnetic Domains: VSM

To examine how the nanospheres curvature changes the magnetic properties of the Fe_3O_4 film, magnetization vs. temperature ($M(T)$) curves in zero-field cooling (ZFC) mode and hysteresis loops ($M(H)$) at different temperatures with an applied in-plane [100] magnetic field were conducted using vibrating sample magnetometer (VSM).

The $M(T)$ curves, shown in **Figure 3a**, are used to detect the Verwey transition (T_V). This transition, which reflects changes in the crystallographic and electronic structure of Fe_3O_4 is highly sensitive to oxygen content, strain, and domain size variations.[28–34] Both the $M(T)$ curves of Fe_3O_4 film on SiO_2 nanospheres and a film grown epitaxially on a flat Nb:STO substrate show a drop in the magnetization at T_V. However, the transition temperature shifts from 120±5 K (flat substrate) to 104±12 K (nanospheres) as shown by the first derivative of the magnetization $\partial M/\partial T$ (inset of Figure 3a). The bulk reference value of 120 K is indicated by the dashed blue line. The lower T_V observed in the film grown on the nanospheres can be attributed to: (1) oxidation state: slight changes in stoichiometry, with $\delta < 0.045$ in $Fe_{3-\delta}O_4$, are known to suppress the Verwey transition when δ values exceeding 0.045.[29] (2) polycrystallinity: the polycrystalline growth on amorphous spheres leads to grain boundaries and antiphase boundaries (APBs), which leads to a lower T_V.[35] (3) finite-size effects: reduced film thickness can suppress long-range charge ordering, further lowering T_V;[32,33] (4) strain: lattice distortions arising from mismatch strain can shift T_V,[29,32,36–38] and (5) surface or interfacial roughness: variations at the Fe_3O_4/substrate or Fe_3O_4/nanosphere surface/interface can locally disturb the lattice or the electron hopping, lowering or even suppressing T_V.[28]

Hysteresis loops ($M(H)$) measured at 300 and 10 K provide additional insights into the magnetic response (Figure 3b,c). At 300 K, the $M(H)$ curve for the film grown on the nanospheres shows a reduced saturation magnetization around ≈2.5 ±0.2 μ_B/f.u. compared to 3.0±0.2 μ_B/f.u. for the flat film. Normalizing the $M(H)$ curve for the film on nanospheres is a challenge due to the variation of film thickness, which covers the nanospheres, and the film not only covers the nanospheres but also extends into the cracks between the nanospheres. Therefore, we assume that the total deposited material is the same as in the flat film since identical growth rate, energy, and deposition time were used, hence, we normalize the magnetization curve using our reference film deposited on flat Nb:STO. The lower saturation magnetization of the film on the nanospheres compared to the flat film is likely due to defects introduced by the nanospheres, a smaller grain size,[39] textured or polycrystalline structure[35] or partial oxidation of Fe_3O_4 to γ-Fe_2O_3 [28] which has a lower saturation magnetization.

At 10 K, below the Verwey transition, significant differences emerge. As observed at 300 K, the saturation magnetization of the nanosphere-grown film remains lower than that of the flat film. However, the coercivity of the nanosphere-grown film increases significantly at 10 K. This drastic change in coercivity and saturation magnetization is attributed to the polycrystallinity of the films on the nanospheres vs. the single crystal epitaxial state. The polycrystallinity introduces random local anisotropy and a higher density of pinning sites.[40,41] Furthermore, structural defects and grain boundaries caused by the curvature of the nanospheres further contribute to these magnetic changes. Curvature-induced thickness variations and magnetic reduced

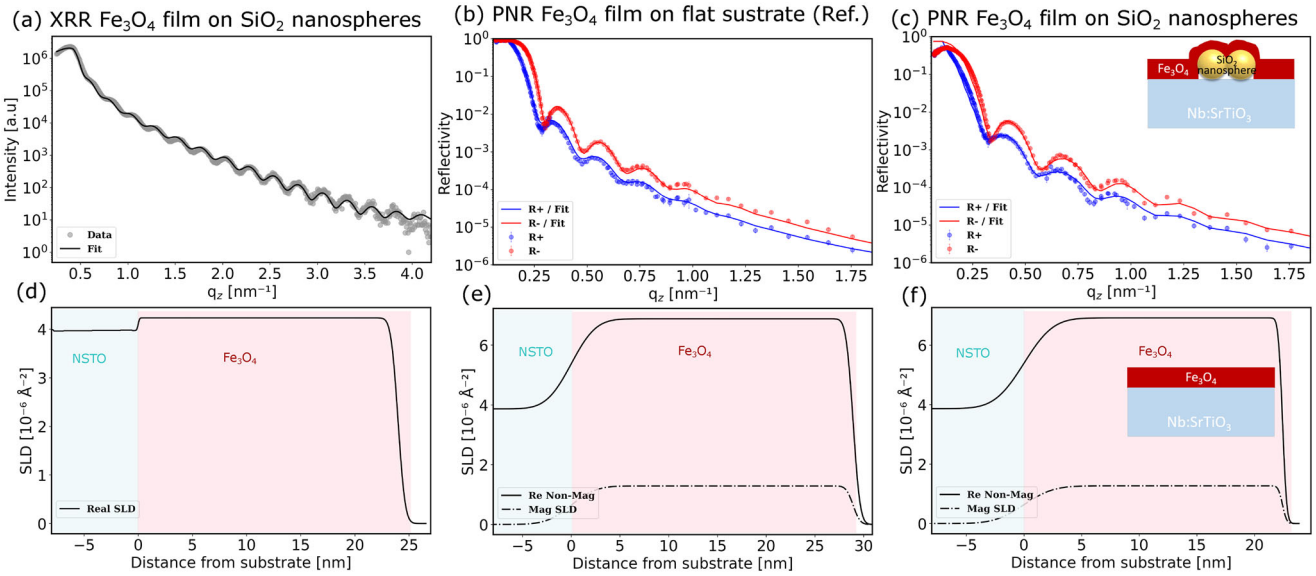

Figure 4. a,d) XRR and scattering length density profile (SLD) from the fit of XRR of 24±2 nm thick Fe_3O_4 film deposited on 174±7 nm diameter SiO_2 nanospheres. b,e) PNR at room temperature and magnetic field of 0.93 T, and scattering length density profiles (nuclear SLD and magnetic SLD) from the fit of the PNR of reference Fe_3O_4 film deposited on flat Nb:STO substrate. c,f) PNR at room temperature and magnetic field of 0.93 T, and scattering length density profiles (nuclear SLD and magnetic SLD) from the fit of the PNR of Fe_3O_4 film deposited on SiO_2 nanospheres. The solid lines show the fit of the data.

domain size also play a crucial role in modifying the magnetic properties.[28,32]

While VSM measurements provide an average magnetic moment over the sample volume, they cannot resolve lateral magnetic fluctuations. To investigate the magnetic depth profile and the in-plane magnetic lateral distribution in Fe_3O_4 nanocaps, PNR and polarized GISANS measurements were conducted, offering complementary insights into the curvature-induced magnetic structure.

2.4. Structural and Magnetic Depth Resolved Analysis: XRR and PNR

X-ray reflectivity (XRR) measurements were performed to examine the thickness, roughness, interface quality, and the structural uniformity of the Fe_3O_4 film deposited on SiO_2 nanospheres assembled on a Nb:$SrTiO_3$ (001) substrate. As shown in **Figure 4a**, the XRR profile shows prominent Kiessig fringes up to high Q_z values, where Q_z is the momentum transfer perpendicular to the sample surface. This indicates low surface roughness, sharp interfaces, and a film thickness 24±2 nm.

To investigate the depth-dependent magnetic structure, polarized neutron reflectivity (PNR) measurements were performed at room temperature under an in-plane [100] magnetic field of 0.93 T for the Fe_3O_4 film on a flat Nb:STO substrate (Figure 4b) and for the Fe_3O_4 film on SiO_2 nanospheres assembled on Nb:STO substrate (Figure 4c). In both samples, R^+ and R^-, the reflectivities of neutrons with spins polarized parallel and antiparallel to the applied magnetic field, respectively, show clear splitting, and strong oscillations confirm in-plane magnetization and high-quality film growth. For the nanosphere-based film, a reduction in scattering intensity at low Q is observed, attributed to diffuse scattering from the SiO_2 nanospheres, as evident in the 2D detector images (see Figure S7, Supporting Information). Despite the surface corrugation introduced by the nanospheres, the overall reflectivity profile closely resembles that of the flat film, suggesting that the dominant contribution to specular reflectivity originates from the flat regions between the nanospheres, consistent with the STEM images (Figure 2a) which show that the Fe_3O_4 film on the nanosphere sample consists of areas deposited directly onto the flat substrate and others deposited on the nanospheres.

The regions where film was deposited on the nanospheres mainly contributed to diffuse scattering, reducing the total specular intensity. Based on reflectivity fitting, approximately 70% of the signal arises from the flat regions. Therefore, the data are modeled using a simple flat-film structure, as illustrated in the schematic inset in Figure 4f, which consists of a $SrTiO_3$ as a substrate and a flat Fe_3O_4 layer. This model successfully reproduces both the PNR and XRR results, and we note that an alternative model incorporating the curvature of the nanospheres was also tested (see Section S4, Supporting Information). These more elaborate curvature-sensitive models produced fits consistent with the flat-film approach, reinforcing that the dominant contribution to the specular signal originates from the flat regions between the nanospheres.

In principle, the reflectivity of the nanosphere-templated film could be described by a two-domain weighted model, combining the flat reference reflectivity with an effective cap contribution scaled by the SEM-derived surface fraction. In practice, however, the caps scatter predominantly into diffuse/off-specular channels, so their specular signal is too weak to allow a reliable decomposition from the present dataset. Moreover, such an incoherent two-domain average would only be valid if flat and nanoparticle-covered regions were laterally separated

on length scales much larger than the beam coherence length (hundreds of micrometers). Since in our samples the domains are intermixed on nanometer–micrometer scales, the specular reflectivity instead reports a lateral average dominated by the flat regions.

To estimate the magnetization of the Fe_3O_4 film on the nanosphere sample, we analyzed the scale factors from the PNR, which normalize the calculated reflectivity to match the measured data. For the flat film sample, the scale factor was set to 1.0, representing a complete magnetically and structurally coherent film. In contrast, the nanosphere-based sample required a reduced scale factor of ≈ 0.72, indicating that only a fraction of the sample contributes coherently to the specular reflectivity. This implies that the flat regions behave magnetically like a continuous film, while the curved caps contribute mainly to diffuse scattering and are weakly detected in PNR.

Magnetically, by fitting PNR, both the flat film and the nanospheres-based films show a moment of approximately 3.4–3.7μ_B/f.u., consistent with room-temperature VSM measurements of the film. This supports the conclusion that the magnetic signal detected by PNR originates primarily from the flat regions of the Fe_3O_4 film.

This finding is consistent with the distinct measurement sensitivities of PNR and VSM. VSM measures the total magnetic moment of the entire sample, including both the flat regions between the nanospheres and the curved Fe_3O_4 caps. In contrast, PNR predominantly detects coherent scattering from laterally uniform layers. As such, the specular PNR signal is primarily sensitive to the flat film regions, with minimal contribution from the curved caps.

To further quantify the magnetic contribution from the curved Fe_3O_4 caps, we compared PNR and VSM results (Figure 3b). VSM measurements yield a magnetization of 3.0±0.2μ_B/f.u. for the flat film and 2.5±0.2μ_B/f.u. for the nanosphere-based film. Using the PNR-derived area fraction of flat film contribution (≈ 0.72), we apply a weighted average:

$$M_{total} = f_{flat}.M_{flat} + f_{NS}.M_{NS},$$

Where f_{flat} = 0.72 is the area fraction of the flat film regions contributing to the reflectivity, f_{NS} = 0.28 is the area fraction of the Fe_3O_4 caps, M_{flat} = 3.0±0.2μ_B/f.u. is the magnetization of the flat film as obtained from VSM, and M_{total} = 2.5±0.2μ_B/f.u. is the total magnetization for the nanospheres based film, and M_{NS} is the magnetization of the Fe_3O_4 caps. From solving the M_{NS}, we find it to be approximately 1.66μ_B/f.u., suggesting that the curved Fe_3O_4 caps possess a weaker magnetization compared to the flat film. This reduction may result from magnetic disorder or the limited sensitivity of PNR to these curved regions due to their contribution to diffuse rather than specular scattering.

In conclusion, XRR and PNR measurements mainly reflect the properties of the flat Fe_3O_4 film regions, with minimal contribution from the film on the nanospheres. Due to the averaging nature of both techniques, local variations in the magnetic and structural properties of the curved caps remain unresolved. To overcome this limitation, laterally sensitive techniques such as GISANS and XMCD-PEEM are employed to probe nanoscale magnetic states and possible oxidation effects in the curved Fe_3O_4 regions, as discussed in the following sections.

2.5. In-Plane Lateral Structural and Magnetic Ordering: GISAXS and GISANS

For investigating the in-plane lateral ordering of the SiO_2 nanospheres and assessing the impact of Fe_3O_4 thin film growth on the degree of nanospheres ordering, Grazing incidence small-angle X-ray scattering (GISAXS) measurements were performed at an incident angle of $\alpha_i \approx 0.23°$ for the SiO_2 nanospheres deposited on the Nb:STO substrate before and after the Fe_3O_4 film growth.

Figure 5a,b shows the GISAXS patterns of the SiO_2 nanospheres before and after film deposition, respectively. Periodic Bragg peaks appear in both GISAXS patterns along the Q_y direction (lateral, in-plane), indicating long-range periodic order of the nanospheres, as shown in the SEM images in Figure 1, forming a 2D hexagonal pattern before and after film deposition. However, some peaks from the hexagonal lattice are hidden within the shoulders of other peaks.

The intensity integration between the two marked red lines from the GISAXS patterns in Figure 5a,b along Q_y is shown in Figure 5c. The Bragg peaks are more intense and sharper before film deposition (red line, Figure 5c). After film deposition (black line, Figure 5c), the Bragg peaks become smeared and slightly shifted compared to the bare silica nanospheres, indicating altered characteristic length scales. The smearing is primarily attributed to a loss of long-range order caused by the Fe_3O_4 deposition, which may disrupt the periodic arrangement of the nanospheres through partial filling of the gaps between them. Additional surface roughness and inhomogeneities introduced by a non-uniform Fe_3O_4 film further contribute to peak broadening. The observed shift in peak positions suggests a modification of interparticle spacing, potentially resulting from compression or material buildup during deposition, as reported in real-time GISAXS studies during metal island growth, where peak movement indicated growth-driven changes in lateral length scales during indium deposition.[42] Moreover, the high scattering length density contrast between Fe_3O_4 and SiO_2 alters the overall scattering profile, contributing to the changes observed in the GISAXS pattern. To further study the effect of curvature on the lateral magnetic fluctuations of the film, GISANS measurements have been conducted.

Polarized GISANS with full polarization analysis was conducted using the D33 instrument. Neutrons were polarized either parallel (+) or anti-parallel (-) to the applied in-plane magnetic field. The GISANS patterns were recorded with an applied in-plane magnetic field along the beam parallel to the [100] direction.

Figure 6a shows the 2D GISANS pattern at 300 K for I^{++} channel, measured at an applied field of -1.2 T, which is around the saturation field of the flat ferrimagnetic film.[28] The pattern shows a specular peak at $Q_z = 0.18$ nm^{-1} with an incident angle of 0.5° and peaks distributed along Q_y give insight into the lateral magnetic and structural ordering, where the magnetic signal shows up as the difference pattern I^{++}-I^{--}.

At both temperatures, 300 and 10 K (Figure 6b,c), a visible difference is observed between I^{++} and I^{--} specular peak and the GISANS peak intensities. This result is due to in-plane magnetism (for comparison Figure 4c). A non-zero spin asymmetry (I^{++} - I^{--}) within the GISANS peaks suggests in-plane lateral

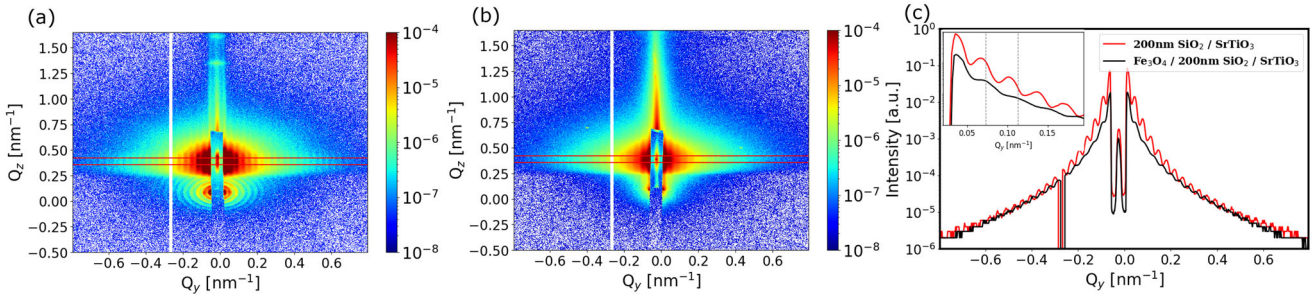

Figure 5. GISAXS patterns of SiO_2 nanospheres at an incident angle of 0.23° a) before film deposition b) after deposition of Fe_3O_4 film. c) Integrated intensity between the two marked red lines in maps (a) and (b).

magnetic fluctuations with a non-zero average magnetization. From the lateral peak positions, we extract the real-space structural and magnetic periodicities from the GISAXS and GISANS data. The peaks are separated by $\Delta Q = 0.04 \pm 0.004$ nm^{-1}, corresponding to a real-space periodicity of $d = 157 \pm 16$ nm, in good agreement with sphere diameter. This confirms that the magnetic periodicity of the Fe_3O_4 caps mirrors the structural periodicity imposed by the nanospheres. Since the structural contribution is present in both the I^{++} and I^{--} channels, it is effectively canceled in the difference plot, isolating the magnetic signal.

The GISANS peaks along Q_y in the NSF measured at 300 and 10 K (Figure 6b,c) remain at the same positions, indicating that the structural periodicity of the nanospheres and the magnetic Fe_3O_4 layer is preserved during cooling through the Verwey transition. This suggests that no significant structural rearrangements or morphological changes occur with temperature variations, which is expected, as atomic rearrangements within the Fe_3O_4 layer in the Angstrom scale would not influence the nanospheres arrangements in the nanometer range.

However, no scattering intensity was observed in the SF channels (I^{+-} and I^{-+}) (Figure S11, Supporting Information) at 300 and 10 K. The absence of SF scattering peaks confirms that there is no detectable out-of-plane magnetic periodicity within the sensitivity of the measurement. This suggests predominantly in-plane magnetic ordering. It is worth noting that GISANS is generally less sensitive to out-of-plane moments compared to in-plane components, especially perpendicular to the applied field direction. Therefore, if the system is near magnetic saturation, as expected under the applied field, any perpendicular magnetic components would be minimal or absent.

GISANS patterns reveal a strong correlation between the lateral magnetization of the Fe_3O_4 films and the underlying nanosphere arrangement. The magnetic periodicity follows the same lateral structural ordering imposed by the nanospheres, and remains stable even at a small field of 0.15 T (Figure S10, Supporting Information).

To further probe the microscopic magnetic domain structure of the Fe_3O_4 film on the SiO_2 nanospheres, XMCD-PEEM measurements were performed, as discussed in the following section.

2.6. Local Lateral Magnetic Domains: XMCD-PEEM

Several questions remain about the microscopic mechanisms responsible for the modified magnetic properties. To investigate these, we employed elemental-specific X-ray photoemission electron microscopy (XPEEM). Before conducting X-ray magnetic circular dichroism photoemission electron microscopy (XMCD-PEEM) measurements, we applied an external in-plane magnetic field of 1.2 T parallel to the sample edge (along the [100] direction). The measurements were then recorded in the remanent state.

XMCD-PEEM was used to obtain the magnetic contrast. This was generated by measuring X-ray absorption (XAS) with right- and left-circular polarization multiple times at the same energy (XMCD = (XAS_{CL} - XAS_{CR})/(XAS_{CL}+XAS_{CR})) as illustrated in the inset of **Figure** 7a. The contrast variations in the image indicate magnetization directions parallel or antiparallel to the wave vector as dictated by sum rules.[43] The XMCD-PEEM image at the L_3 resonance (E = 705.5 eV) is shown in Figure 7a. We can

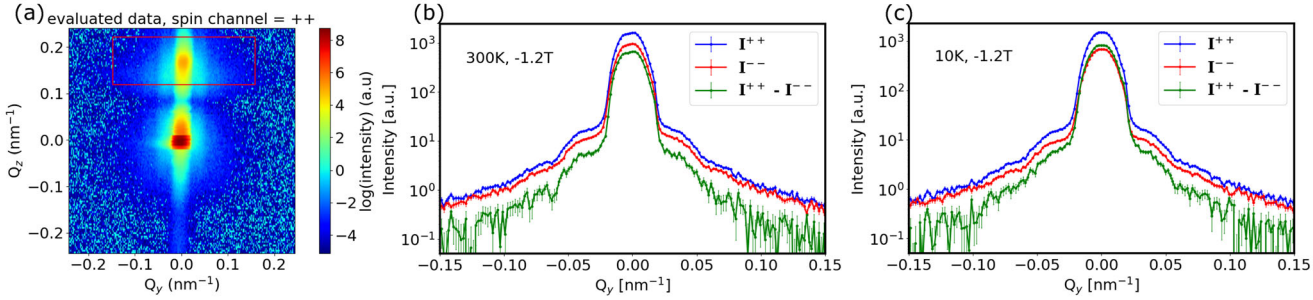

Figure 6. GISANS measurements of Fe_3O_4 film deposited on SiO_2 nanospheres with in-plane [100] magnetic field of -1.2 T: a) 2D image at room temperature of I^{++} spin channel with red square marks the integrated intensity area used for calculating I^{++}, I^{--} and $I^{++} - I^{--}$ b) at room temperature, and c) at 10 K.

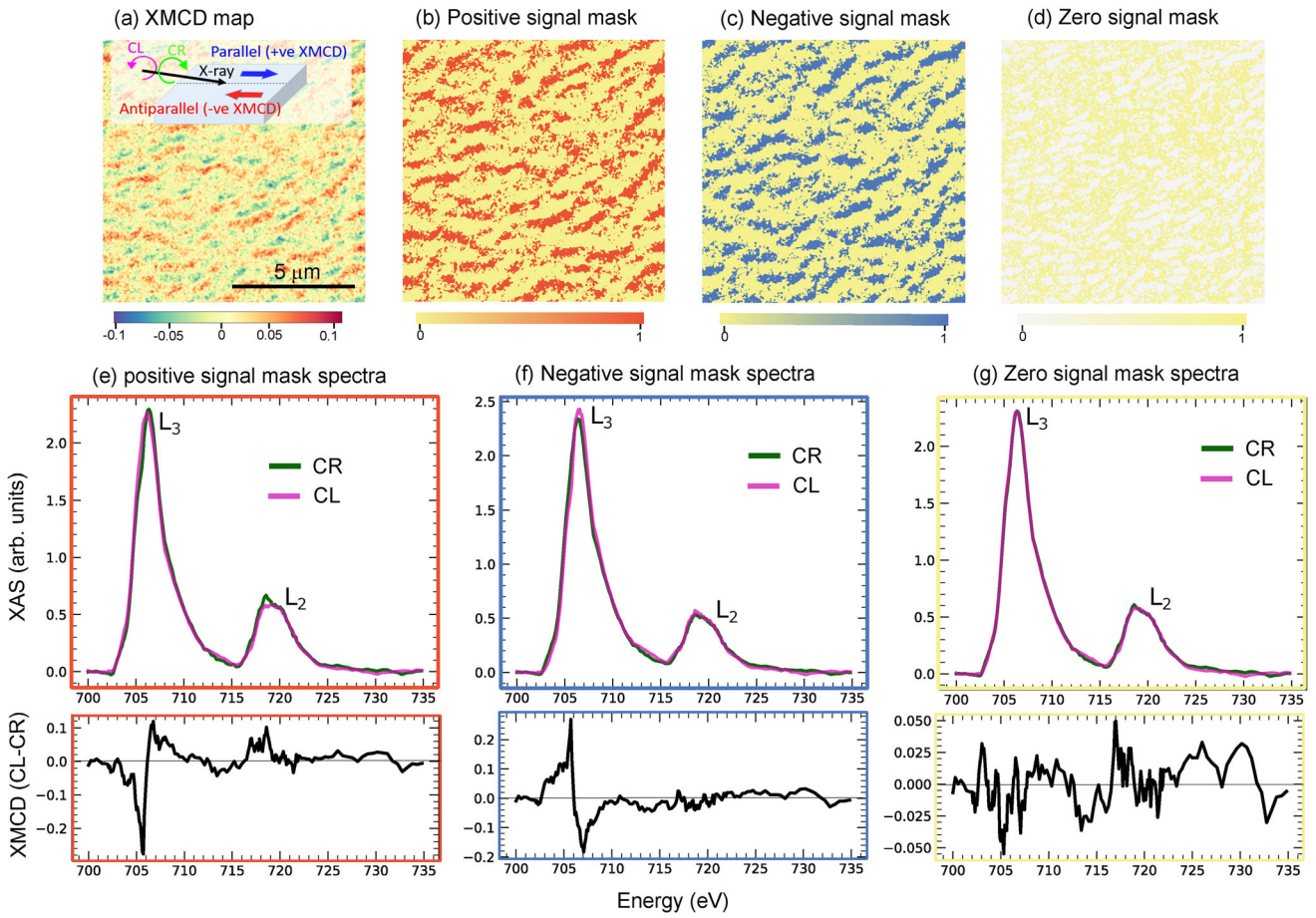

Figure 7. a) XMCD-PEEM image (E = 705.5 eV), b–d) threshold masks identifying three regions of magnetic domains in the image e–g) Fe $L_{2,3}$-edge XAS and XMCD spectra of the three magnetic domains identified by the mask.

identify three types of domains in the image, which are: positive XMCD domains in red, negative XMCD domains in blue and zero XMCD domains in yellow. The XMCD signals of the three identified magnetic domains were obtained using a threshold intensity mask as shown in Figure 7b–d (For more details, see Section S6, Supporting Information). The first is the positive XMCD domains and are color-coded in red (Figure 7b). The magnetic moment of these domains is mainly oriented antiparallel to the orientation of the X-ray beam. The second is the negative XMCD domains and are color-coded in blue (Figure 7c). The magnetic moment of these domains is mainly oriented parallel to the orientation of the X-ray beam. Finally, zero XMCD signal domains can also be seen and are color-coded in yellow (Figure 7d). These domains either have no magnetic moment or their magnetic moment is oriented perpendicular to the X-ray beam and can not be detected which is the likely scenario.

To reveal more details about the chemical and magnetic structure of each domain, we measured the full X-ray absorption spectroscopy (XAS) and XMCD spectra by recording a series of images at different photon energies across the Fe $L_{2,3}$-edge using CR and CL polarized light. In Figure 7e–g, the CR and CL XAS spectra of each domain were obtained by averaging the intensity from each domain separately using the masks shown in Figure 7b–d. The resulting XAS spectra for the three domains are very similar and exhibit Fe $L_{2,3}$-edge features, reflecting the mixed contributions of Fe^{2+} and Fe^{3+} in the octahedral sites and Fe^{3+} in the tetrahedral sites. By comparing the XAS spectra of the Fe_3O_4 film on the SiO_2 nanospheres to a reference Fe_3O_4 film on a flat Nb:STO substrate sample (Figure S13, Supporting Information), slight differences in the pre-edge peak intensities and the L_3 peak-to-shoulder ratio are observed. These variations hint at a minor deviation from stoichiometry in the Fe_3O_4 film on SiO_2 nanospheres sample. On the other hand, a clear XMCD signal can be seen (bottom row in Figure 7e–g) for the positive and negative domains, which inverts, referring to the magnetic orientation within the domains.

The XPEEM measurements have been performed on a region of the sample that includes both: the Fe_3O_4 film deposited on SiO_2 nanospheres and the film on the flat Nb:STO substrate, as shown in the SEM image **Figure** 8a. To correlate the magnetic texture with the underlying morphology, we generated structural masks (Figure 8b–d) using the images contrast measured before the Fe absorption edge. At this energy, the contrast in the image relates mainly to the morphology with lower intensity regions corresponding to Fe_3O_4 film on the Nb:STO substrate (Figure 8b) and higher intensity regions corresponding to Fe_3O_4 on nanospheres (Figure 8c) (For more details about the calculated masks, see Section S6, Supporting Information). In

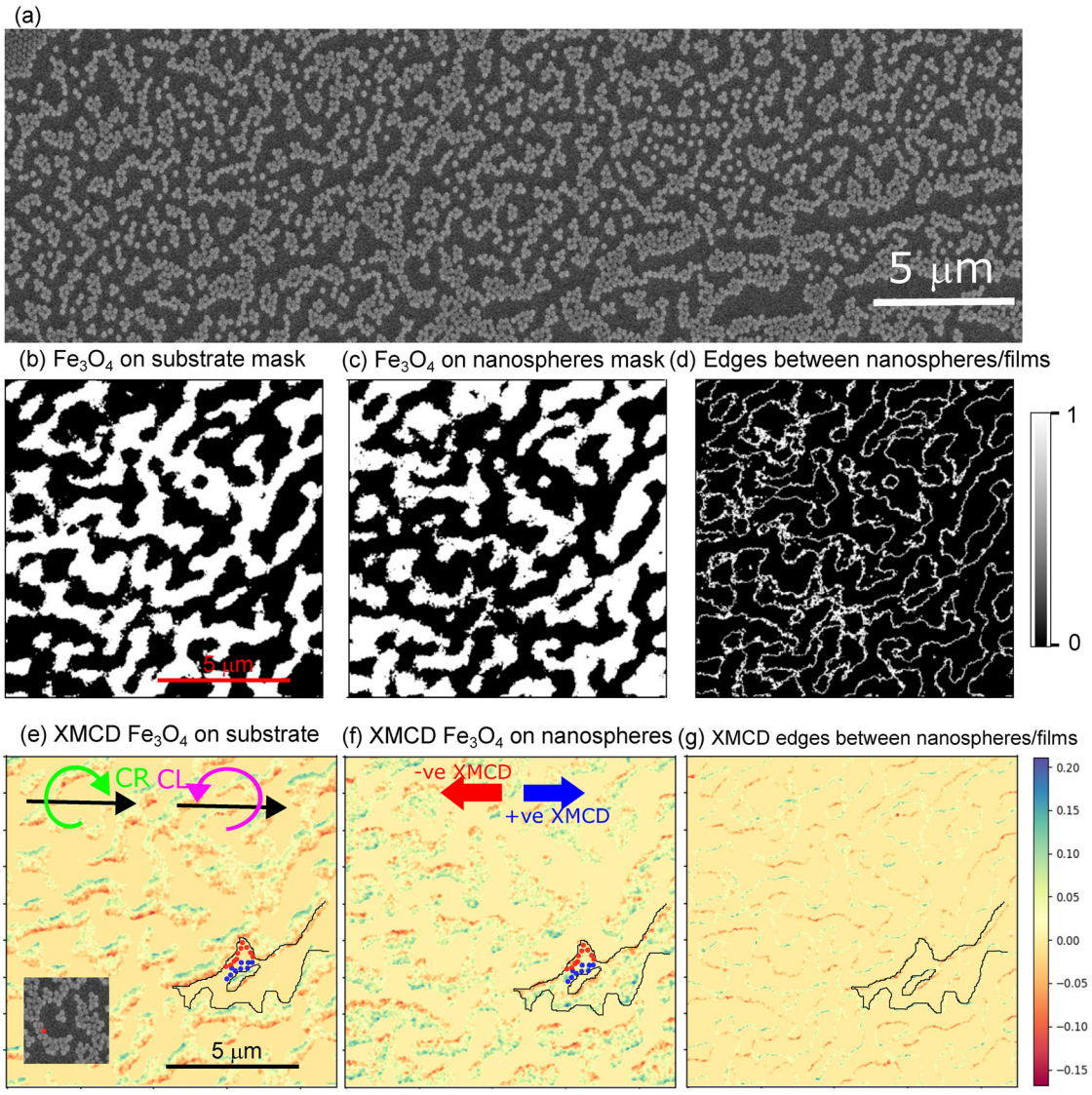

Figure 8. a) SEM image of Fe_3O_4 film on SiO_2 nanospheres in a region with partial coverage. b–d) Masks identifying three structural regions in the image: (b) Fe_3O_4 deposited on the flat Nb:STO substrate, (c) Fe_3O_4 deposited on the SiO_2 nanospheres, and (d) border region in between. e–g) XMCD contrast for the three structural regions as identified in (b–d): Red domains are positive XMCD regions, blue are negative XMCD, and yellow are zero XMCD regions for the specific mask applied.

addition, the border region between both is identified and masked in Figure 8d. The multiplication of both the magnetic and structural masks identifies magnetic domains corresponding to the Fe_3O_4 film on the Nb:STO substrate (Figure 8e), on nanospheres (Figure 8f), and in the border regions between them (Figure 8g). In the nanospheres-covered region, we observe micrometer-scale patches with a meandering pattern. One example patch is highlighted in Figure 8e–g, where the magnetic orientation at the edge of the nanosphere island aligns with that of the neighboring Fe_3O_4 film on the flat substrate, suggesting continuity of magnetic domains (e.g., red neighboring red). This magnetic domain alignment extends across the border region (Figure 8g), indicating that the Fe_3O_4 film on the nanospheres and that on the substrate are magnetically coupled rather than behaving as independent regions. This finding is unexpected, as the polycrystalline Fe_3O_4 film on the nanospheres is not anticipated to exhibit a preferred magnetization direction, in contrast to the epitaxial Fe_3O_4 film on the Nb:STO substrate, which has a known easy axis along the [100] direction.[38] The Fe_3O_4 layer remains almost continuous across the nanospheres and the flat substrate, connecting neighboring caps through the planar film. This continuous network allows for exchange-mediated correlations between the nanocaps and the flat regions. Therefore, the observed domain continuity suggests that magnetic texture from the epitaxial flat film may be transferred to the nanosphere region via correlated domain behavior across flat and curved regions. As a reference, the Fe_3O_4 film deposited on a continuous flat substrate shows single-domain behavior (Figure S14, Supporting Information), further supporting the conclusion that both the nanosphere and flat regions can influence and even reverse domain

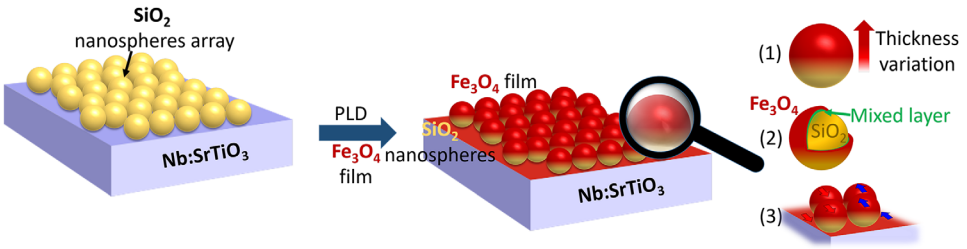

Figure 9. Schematics of the Fe_3O_4 film/SiO_2 nanospheres/Nb:$SrTiO_3$ substrate and three possible cases for the structural and magnetic distribution across the Fe_3O_4 caps: (1) thickness variation, (2) interfacial chemical and magnetic structure, and (3) induced domain texture.

orientations in their immediate neighbors, reflecting the correlated domain behavior between these two regions.

In conclusion, while the resolution of the experiment does not allow for resolving magnetic textures at the scale of individual nanospheres, the almost continuous growth of the Fe_3O_4 film across both the nanospheres and the valleys between nanospheres likely facilitates the interactions between these two regions. This correlation is presumed to contribute to the coherent magnetic texture observed across the nanosphere and flat regions. XMCD demonstrates correlated domain behavior across flat and curved regions, while the underlying mechanism may involve a combination of partial structural continuity and dipolar coupling. A definitive distinction between these contributions would require further studies, such as micromagnetic simulations or tomography-based structural characterization, which we propose for future work.

2.7. Discussion

After characterizing the Fe_3O_4 film/SiO_2 nanospheres sample using a combination of techniques, we found that the Fe_3O_4 film conforms to the nanospheres, forming dense, curved nanocaps. Based on our observations, three possible mechanisms may govern the distribution of structural and magnetic domains: (1) thickness variation, (2) interfacial chemical and magnetic structure, and (3) induced domain texture, as shown in **Figure 9**.

(1) Thickness Variation

STEM measurements reveal that the film thickness varies along the curved surface of individual nanospheres. This local variation can significantly influence magnetic domain formation, as shown in our earlier work, demonstrating that reducing film thickness alters both the magnetic and chemical properties of Fe_3O_4 .[28] Such variations may contribute to the deviation observed in the XMCD spectrum from the characteristic "W"-shaped profile typically associated with Fe_3O_4.

(2) Interfacial Chemical and Magnetic Structure

STEM images suggest the presence of a structural, chemical, or morphological mixing region between the Fe_3O_4 film and the SiO_2 nanospheres, however, its origin and chemical or magnetic structure remain uncertain. Depth-resolved PNR lacks the sensitivity to distinguish local variations in the curved film regions and thus does not provide information about the interface between the Fe_3O_4 film and the SiO_2 nanospheres, as reflectivity from curved regions contributes to diffuse scattering. XAS spectra extracted from XPEEM data show slight chemical and structural differences between the curved Fe_3O_4 film and the reference Fe_3O_4 film, but no definitive evidence of significant changes, either chemical or magnetic, at the interfaces was observed. However, the XMCD signals of both the curved and flat regions exhibit distinct differences in comparison to the reference thin film (see Section S6, Supporting Information) and to previously reported spectra in the literature.[44] Further studies are needed to disentangle geometric effects from potential interfacial intermixing.

(3) Induced Domain Texture

Combined PNR and VSM measurements indicate that the magnetic response of the nanosphere-based film originates mainly from the flat film regions, with smaller total magnetization from the curved caps. GISANS measurements confirm that the Fe_3O_4 film conforms to the nanosphere curvature and possesses an in-plane magnetic structure, with no out-of-plane magnetic moments detected. XMCD-PEEM images reveal the presence of reversed magnetic domains across the nanosphere-covered regions, which appear continuous with those in the neighboring flat Fe_3O_4 film on the substrate. However, the magnitude of the XMCD signal of the Fe_3O_4 on nanosphere curvature is nearly half of that from the flat Fe_3O_4 film, confirming that the main magnetic response originated from the Fe_3O_4 film. This is further supported by the STEM data, which shows that the Fe_3O_4 film grows continuously over the nanospheres and into the valleys between them with local gaps at the curved–flat interfaces. Such partial structural continuity likely facilitates correlated domain behavior between the nanocaps and the surrounding flat regions, giving rise to an induced, correlated magnetic domain texture across the entire film. Additionally, both curvature and polycrystallinity play complementary roles in the magnetic domain texture: polycrystallinity (with its associated grain boundaries and random anisotropy) most strongly affects the magnetization magnitude and coercivity, while curvature primarily governs the lateral arrangement and domain shape. To quantify both contributions, this would require systematic studies across different nanosphere diameters and controlled epitaxial vs. polycrystalline growth, which are important directions for future work.

3. Conclusion

Understanding and tailoring the magnetic and atomic structures of geometrically complex oxide films is a crucial step toward unlocking new functionalities for oxide spintronics. In this study, Fe_3O_4 thin films were grown on self-assembled SiO_2 nanospheres supported by Nb:$SrTiO_3$ substrates to explore how nanoscale morphology influences magnetic behavior. The film

conforms to the nanosphere template, forming polycrystalline caps with varying thickness, while maintaining epitaxial growth in the flat regions. This structural variation leads to reduced net magnetization in the nanosphere-covered areas, as confirmed by VSM and PNR. However, XMCD-PEEM reveals continuous in-plane magnetic domain textures that span both curved and flat regions, indicating correlated domain behavior across topographically different areas. Our findings therefore reflect the combined influence of local curvature and polycrystalline morphology within a quasi-continuous cap-and-bridge film, rather than curvature effects in isolation. These findings establish nanoscale morphology as a tool for modulating magnetism in oxide thin films, which contribute to the emerging field of curvilinear spintronics.

4. Experimental Details

Magnetite (Fe_3O_4) thin films of 24±2 nm thickness were deposited using pulsed laser deposition (PLD) on two types of surfaces: 1) epi-polished Nb-doped TiO_2-terminated $SrTiO_3$ (001) (Nb:STO) substrates, serving as a reference, and 2) arrays of silica nanospheres with an average diameter of 174±7 nm as obtained from SAXS measurement (Figure S1, Supporting Information), first deposited on Nb:STO substrates using a simple drop-casting method, as outlined in Qdemat et al.[45] Both types of samples were transferred to the PLD chamber for the growth of magnetite thin films. The deposition was performed using a rotating target of Fe_2O_3 with the substrates held at a temperature of $T = 500$°C. During the growth, the oxygen background pressure was kept at 2×10^{-6} mbar, and the laser fluence and repetition rate were set to 1.5 J/cm^2 and 5 Hz, respectively. These parameters have been chosen based on our previous studies[26–28] as they result in thin films of magnetite on STO with superior crystalline and magnetic properties. In pulsed laser deposition, the ablation plume has a broad angular distribution, which enables deposition both on the nanosphere tops and around their sides. This geometry naturally leads to local thickness variations, and small gaps are likely to persist near the interfaces between the nanosphere and the underlying flat film on the substrate.

The Fe_3O_4 films deposited on SiO_2 nanospheres arrays on Nb:STO substrates were first characterized by scanning electron microscopy (SEM, Hitachi SU8000) to examine the ordering of the nanospheres before and after film deposition. The cross-sectional structure of the sample with atomic resolution has been investigated by means of transmission electron microscopy (TEM) and scanning transmission electron microscopy (STEM). A JEOL JEM-2010F microscope, equipped with a Schottky field emission gun and operating at 200 keV, was used to conduct conventional TEM (CTEM) investigations in parallel beam and selected area electron diffraction (SAED). STEM analyses have been performed by using a JEOL ARM200F Cs-corrected microscope, which is equipped with a cold-field emission gun and operating at 200 keV. Micrographs were acquired in Z-contrast mode by High-Angle Annular Dark Field (HAADF) and in diffraction contrast by Low-Angle Annular Dark Field (LAADF).

Magnetic properties, i.e., saturation magnetization and Verwey transition of the magnetite films on SiO_2 nanospheres as well as on the Nb:STO substrate, were investigated by a vibrating sample magnetometer (VSM) using a Quantum Design Dynacool physical properties measurement system (PPMS). Magnetic moment versus temperature was measured in zero-field cooling (ZFC) mode with an applied field of 500 Oe. Hysteresis loops were recorded at a magnetic field of ±5T along the in-plane [100]-axis at temperatures of 10 and 300 K.

To explore the structural depth profile of Fe_3O_4 film on SiO_2 nanospheres, X-ray reflectivity (XRR, Brucker D8) was measured with Cu K_α ($\lambda = 0.154$ nm) radiation to obtain the surface roughness and film thickness. To study the depth profile of magnetism at the interface, the interfacial magnetic configuration, and the stoichiometric gradient change across the Fe_3O_4 film and the interface with the SiO_2 spheres, we used a depth-sensitive polarized neutron reflectivity (PNR) technique. PNR measurements were carried out at D17, at the Institut Laue-Langevin (ILL), Grenoble, France[46] at room temperature and under an applied in-plane [100] magnetic field of 0.93 T. The data has been automatically corrected for polarization efficiency using TOF-NR.[47]

Grazing incidence small-angle X-ray scattering (GISAXS) measurements were performed to investigate the in-plane lateral ordering of the nanospheres. GISAXS measurements were carried out at the diffractometer Gallium Anode Low-Angle X-ray Instrument GALAXI[48] using a monochromatic X-ray beam with a wavelength of $\lambda = 0.1314$ nm and a beam with a cross-section at the sample of 0.7×0.7 mm^2. These measurements were carried out at incident angle α_i of 0.23° and the scattering pattern is recorded by a Pilatus 1M 2D position sensitive detector with 169 × 179 mm^2 active area at a sample-detector distance of 3528 mm.

For an investigation of in-plane magnetic lateral correlations and magnetic domain formation, polarized grazing-incidence small-angle neutron scattering (GISANS) with full polarization analysis was performed at the D33 beamline (proposal no. 554404) at the Institut Laue-Langevin (ILL), Grenoble, France.[49] The measurements were conducted at 300K and 10K using neutrons of a wavelength $\lambda = 6$ Å at an incident angle of 0.5°. Data were taken for three different magnetic states with in-plane [100]-axis magnetic field: (i) in magnetic saturation (1.2 T), (ii) at 0.15 T from +1.2 T, and (iii) at 0.15 T from −1.2 T. We have used a supermirror polarizer and a ^{3}He-cell analyzer for the polarization analysis of neutrons. All data have been reduced considering the ^{3}He-cell time-dependence and all polarization component efficiencies.

In order to analyze microscopic magnetic domain configurations, X-ray magnetic circular dichroism photoemission electron microscopy (XMCD-PEEM) was conducted on the HERMES beamline[50] at the SOLEIL synchrotron, Paris, France. The XMCD measurements were performed at room temperature across Fe $L_{2,3}$-edge with an angle of $\theta = 16°$ between the beam axis and the surface plane of the sample and beam size of 50*50 μm^2, enabling the capture of remanent magnetic domain structures in the absence of an external magnetic field with estimated spatial resolution of 100 nm, using films that were pre-magnetized ex-situ with in-plane [100] magnetic field of 1.2 T.

Supporting Information

Supporting Information is available from the Wiley Online Library or from the author.

Acknowledgements

The authors would like to acknowledge R. Dittmann for providing the PLD setup and X-ray Reflectivity (XRR) at PGI7-FZJ. Special thanks to E. Kentzinger and U. Rücker for their help with GALAXI at FZJ. The authors thank E. Kentzinger and S. Tober for the fruitful discussions regarding GISAXS, and N. Seidel for assistance with SEM and GISANS beamtime. Special thanks to J. Buitenhuis for preparing the high-quality SiO_2 nanospheres. The authors thank M. Faley for the discussions regarding TEM. The authors acknowledge SOLEIL for the provision of synchrotron radiation facilities and authors would like to thank S. Stanescu, R. Belkhou, and S. Swaraj for assistance in using beamline HERMES. M.H.H. expresses gratitude to W. Esmail for his assistance in developing the PEEM machine learning code. The authors thank K. Friese for the valuable discussions. M.H.H. thanks the Tasso Springer Fellowship provided by JCNS-2 for the funding. A.M.M. acknowledges financial support by the national project, BEYOND NANO Upgrade (CUP G66J17000350007) and by NextGenerationEU, M4C2, within the PNRR project NFFA-DI, CUP B53C22004310006, IR0000015, having benefited from the access provided by CNR-IMM@CT in Catania. The authors acknowledge the provision of beamtime on the D33 and D17 instruments at the Institute Laue-Langevin. H.E. acknowledges the Rubicon funding from NWO (Grant 019.201EN.010 entitled Shining Light on Self-Assembled Bimagnetic Ferrofluids).

Conflict of Interest

The authors declare no conflict of interest.

Author Contributions

M.H.H. wrote the original manuscript, determined the research direction, and conceptualized the experiments, including sample preparation and characterization experiments and analysis of XRR, XRD, SEM, VSM, GISAXS, GISANS, and XPEEM experiments. Y.X. contributed to SEM, VSM, XRR fitting, XPEEM beamtime, and GISANS beamtime; H.E. participated in the XPEEM beamtime, analyzed the XPEEM measurements, performed crystal field multiplet calculations and beam tracing calculations; M.Z. and A.M.M. performed FIB/TEM/STEM experiments and data analysis. A.S. and A.B. handled GISANS data reduction and discussion; V.O.L. and C.Y. participated in XPEEM beamtime; C.B.M. engaged in GISANS discussions; N.J.S. served as the beam scientist for D33 and reviewed the GISANS section. O.P. participated in VSM discussions; T.B. provided supervision. T.S., as the beam scientist for D17, reviewed the PNR and GISANS sections and provided input for the overall conclusions. A.Q. assisted with SEM, GISAXS, GISANS, XPEEM beamtime and conducted the PNR experiment and PNR data reduction and fitting; A.Q. assisted in manuscript preparation, and all authors reviewed and approved the final version.

Data Availability Statement

The data that support the findings of this study are available from the corresponding author upon reasonable request.

Keywords

Fe_3O_4 thin film, nanoscale topography, oxide interfaces, SiO_2 nanospheres, XMCD-PEEM

Received: July 18, 2025
Revised: October 3, 2025
Published online:

[1] J. Xu, Z. Luo, L. Chen, X. Zhou, H. Zhang, Y. Zheng, L. Wei, *Mater. Horiz.* **2024**, *11*, 4015.
[2] R. Streubel, E. Y. Tsymbal, P. Fischer, *J. Appl. Phys.* **2021**, *129*, 210902.
[3] M. Albrecht, G. Hu, I. Guhr, T. Ulbrich, J. Boneberg, P. Leiderer, G. Schatz, *Nat. Mater.* **2005**, *4*, 203.
[4] J. Fullerton, A. R. C. McCray, A. K. Petford-Long, C. Phatak, *Nano Lett.* **2024**, *24*, 2481.
[5] R. Streubel, F. Kronast, P. Fischer, D. Parkinson, O. G. Schmidt, D. Makarov, *Nat. Commun.* **2015**, *6*, 7612.
[6] A. Fernández-Pacheco, R. Streubel, O. Fruchart, R. Hertel, P. Fischer, R. P. Cowburn, *Nat. Commun.* **2017**, *8*, 15756.
[7] R. Streubel, P. Fischer, F. Kronast, V. P. Kravchuk, D. D. Sheka, Y. Gaididei, O. G. Schmidt, D. Makarov, *J. Phys. D: Appl. Phys.* **2016**, *49*, 363001.
[8] D. D. Sheka, O. V. Pylypovskyi, P. Landeros, Y. Gaididei, A. Kákay, D. Makarov, *Commun. Phys.* **2020**, *3*, 128.
[9] V. P. Kravchuk, D. D. Sheka, A. Kákay, O. M. Volkov, U. K. Rößler, J. van den Brink, D. Makarov, Y. Gaididei, *Phys. Rev. Lett.* **2018**, *120*, 067201.
[10] A. Sharma, J. Tripathi, S. Tripathi, Y. Kumar, K. Ugochukwu, D. Kumar, M. Gupta, R. Chaudhary, *J. Magn. Magn. Mater.* **2020**, *510*, 166599.
[11] J. Krempaský, L. Šmejkal, S. W. D'Souza, M. Hajlaoui, G. Springholz, K. Uhlířová, F. Alarab, P. C. Constantinou, V. Strocov, D. Usanov, W. R. Pudelko, R. González-Hernández, A. Birk Hellenes, Z. Jansa, H. Reichlová, Z. Šobáň, R. D. Gonzalez Betancourt, P. Wadley, J. Sinova, D. Kriegner, J. Minár, J. H. Dil, T. Jungwirth, *Nature* **2024**, *626*, 517.
[12] K. Hofhuis, C. F. Petersen, M. Saccone, S. Dhuey, A. Kleibert, S. van Dijken, A. Farhan, *Phys. Rev. B* **2021**, *104*, 014409.
[13] M. M. Soares, E. de Biasi, L. N. Coelho, M. C. dos Santos, F. S. de Menezes, M. Knobel, L. C. Sampaio, F. Garcia, *Phys. Rev. B* **2008**, *77*, 224405.
[14] J. Yang, N. Yang, Y. Wang, Y. Zhang, Y. Zhang, Y. Liu, M. Wei, Y. Yang, R. Wang, S. Yang, *Solid State Commun.* **2011**, *151*, 1428.
[15] C. Prakash, A. Dixit, *ACS Appl. Electron. Mater.* **2022**, *4*, 5763.
[16] S. Porro, K. Bejtka, A. Jasmin, M. Fontana, G. Milano, A. Chiolerio, C. F. Pirri, C. Ricciardi, *Nanotechnology* **2018**, *29*, 495201.
[17] Y. Gaididei, V. P. Kravchuk, D. D. Sheka, *Phys. Rev. Lett.* **2014**, *112*, 257203.
[18] C. H. Marrows, J. Barker, T. A. Moore, T. Moorsom, *npj Spintronics* **2024**, *2*, 12.
[19] D. Makarov, D. D. Sheka, editors, *Curvilinear Micromagnetism: From Fundamentals to Applications*, vol. 134 of *Topics in Applied Physics*, Springer Cham, 1 ed., **2022**.
[20] D. D. Sheka, *Appl. Phys. Lett.* **2021**, *118*, 230502.
[21] D. Makarov, O. M. Volkov, A. Kákay, O. V. Pylypovskyi, B. Budinská, O. V. Dobrovolskiy, *Adv. Mater.* **2022**, *34*, 2101758.
[22] T. Ishibe, Y. Uematsu, N. Naruse, Y. Mera, Y. Nakamura, *Appl. Phys. Lett.* **2020**, *116*, 181601.
[23] T. Ishibe, T. Kurokawa, N. Naruse, Y. Nakamura, *Appl. Phys. Lett.* **2018**, *113*, 141601.
[24] J. M. D. Coey, *Magnetism and Magnetic Materials*, Cambridge University Press, Cambridge **2010**.
[25] V. N. Antonov, B. N. Harmon, A. N. Yaresko, *Phys. Rev. B* **2003**, *67*, 024417.
[26] M. H. Hamed, D. N. Mueller, M. Müller, *Appl. Surf. Sci. Adv.* **2021**, *6*, 100132.
[27] M. H. Hamed, D. N. Mueller, M. Müller, *J. Mater. Chem. C* **2020**, *8*, 1335.
[28] M. H. Hamed, R. A. Hinz, P. Lömker, M. Wilhelm, A. Gloskovskii, P. Bencok, C. Schmitz-Antoniak, H. Elnaggar, C. M. Schneider, M. Müller, *ACS Appl. Mater. Interfaces* **2019**, *11*, 7576.
[29] R. Aragón, D. J. Buttrey, J. P. Shepherd, J. M. Honig, *Phys. Rev. B* **1985**, *31*, 430.
[30] J. A. Moyer, S. Lee, P. Schiffer, L. W. Martin, *Phys. Rev. B* **2015**, *91*, 064413.
[31] C. Schmitz-Antoniak, D. Schmitz, A. Warland, M. Darbandi, S. Haldar, S. Bhandary, B. Sanyal, O. Eriksson, H. Wende, *Ann. Phys.* **2018**, *530*, 1700363.
[32] X. H. Liu, A. D. Rata, C. F. Chang, A. C. Komarek, L. H. Tjeng, *Phys. Rev. B* **2014**, *90*, 125142.
[33] S. Alraddadi, W. Hines, T. Yilmaz, G. D. Gu, B. Sinkovic, *J. Phys.: Condens. Matter* **2016**, *28*, 115402.
[34] G. Perversi, E. Pachoud, J. Cumby, J. M. Hudspeth, J. P. Wright, S. A. J. Kimber, J. P. Attfield, *Nat. Commun.* **2019**, *10*, 2857.
[35] H. Liu, E. Y. Jiang, R. K. Zheng, H. L. Bai, *Phys. Status Solidi A* **2004**, *201*, 739.
[36] J. Dho, B.-g. Kim, S. Ki, *J. Appl. Phys.* **2015**, *117*, 163904.
[37] M. B. Yazdi, M. Major, A. Wildes, F. Wilhelm, A. Rogalev, W. Donner, L. Alff, *Phys. Rev. B* **2016**, *93*, 014439.
[38] J. L. F. Cuñado, J. Camarero, F. J. Pedrosa, N. M. Nemes, M. Sanz, M. Oujja, E. Rebollar, J. F. Marco, J. de la Figuera, M. Monti, M. Castillejo, T. Feher, B. Nafradi, L. Forró, A. Bollero, *Nanoscale* **2019**, *11*, 19870.
[39] Q. Li, C. W. Kartikowati, S. Horie, T. Ogi, T. Iwaki, K. Okuyama, *Sci. Rep.* **2017**, *7*, 9894.

[40] A. M. Abdelgawad, N. Nambiar, M. Bapna, H. Chen, S. A. Majetich, *AIP Adv.* **2018**, *8*, 056321.
[41] A. Mourkas, A. Zarlaha, N. Kourkoumelis, I. Panagiotopoulos, *J. Magn. Magn. Mater.* **2021**, *524*, 167676.
[42] A. Demasi, M. G. Rainville, J. Ludwig, F. Karl, *J. Vac. Sci. Technol., A* **2015**, *33*, 021406.
[43] P. Carra, *J. Electron Spectrosc. Relat. Phenom.* **1997**, *86*, 139.
[44] H. Elnaggar, R. Wang, M. Ghiasi, M. Ya nez, M. U. Delgado-Jaime, M. H. Hamed, A. Juhin, S. S. Dhesi, F. de Groot, *Phys. Rev. Mater.* **2020**, *4*, 024415.
[45] A. Qdemat, E. Kentzinger, J. Buitenhuis, U. Rücker, M. Ganeva, T. Brückel, *RSC Adv.* **2020**, *10*, 18339.
[46] T. Saerbeck, R. Cubitt, A. Wildes, G. Manzin, K. H. Andersen, P. Gutfreund, *J. Appl. Crystallogr.* **2018**, *51*, 249.
[47] P. Gutfreund, T. Saerbeck, M. A. Gonzalez, E. Pellegrini, M. Laver, C. Dewhurst, R. Cubitt, *J. Appl. Crystallogr.* **2018**, *51*, 606.
[48] E. Kentzinger, M. Krutyeva, U. Rücker, *J. Large-scale Res. Facil. JLSRF* **2016**, *2*, A61.
[49] C. D. Dewhurst, I. Grillo, D. Honecker, M. Bonnaud, M. Jacques, C. Amrouni, A. Perillo-Marcone, G. Manzin, R. Cubitt, *J. Appl. Cryst.* **2016**, *49*, 1.
[50] R. Belkhou, S. Stanescu, S. Swaraj, A. Besson, M. Ledoux, M. Hajlaoui, D. Dalle, *J. Synchrotron Radiat.* **2015**, *22*, 968.